

Direct Recycling of Hot-Deformed Nd–Fe–B Magnet Scrap by Field-Assisted Sintering Technology

Monica Keszler, Felix Grosswendt, Anna-Caroline Assmann, Martin Kregel, Fernando Maccari, Oliver Gutfleisch, Doris Sebold, Olivier Guillon, Sebastian Weber, and Martin Bram*


Recycling of Nd–Fe–B magnets is an ongoing challenge regarding circular economy. State-of-the-art magnet production methods, such as hot deformation, have limitations with respect to direct recycling of magnet scrap particles that differ from pristine melt-spun Nd–Fe–B powder. Recent work has shown that a combination of presintering by field-assisted sintering technology/spark plasma sintering (FAST/SPS) and hot deformation by flash spark plasma sintering (flash SPS) has the potential to directly produce Nd–Fe–B magnets from 100% scrap material. Both processes have the capability to adjust and monitor process parameters closely, resulting in recycled magnets with properties similar to commercial magnets but made directly from crushed and recycled Nd–Fe–B powder that partially or completely replaces pristine melt-spun Nd–Fe–B powder. Herein, a systematic study is done inserting recycled magnet particles into a flash SPS deformed magnet, considering the effects of different weight percentages of scrap material of varied particle size fractions. In some cases, coercivity H_{cJ} of $>1400 \text{ kAm}^{-1}$ and remanence B_r of 1.1 T can be achieved with 20 wt% scrap material. The relationship between particle size fraction, oxygen uptake, and percentage of recycle in a final magnet are all explored and discussed with respect to magnets made from pristine material.

1. Introduction

Nd–Fe–B-based magnets have the highest maximum energy product, $(BH)_{\text{max}}$ (theoretical: 512 kJ m^{-3}), of all current market magnet materials around room temperature, making them prime for use in a wide variety of applications, including, green energy production via wind turbines; vehicles including hybrid electric vehicles, electric vehicles, and e-bikes; as well as a wide variety of consumer electronics including computers.^[1–3] These magnets are often tuned to specific properties with the addition of heavy-rare-earth elements (REEs), such as Dy and Tb.^[4] Addition of these elements leads to a variety of improvements, such as enhanced coercivity, H_{cJ} , which is the magnet's resistance to change in magnetization and higher-temperature tolerance.^[5] Most of primary REE mining is localized to just a few countries, such as China, USA, Australia, and India, and it continues to be difficult to meet the growing demand for REEs in modern technology. However, the amount of e-waste rich in REEs, including doped Nd–Fe–B magnets, is rising globally, with

M. Keszler, D. Sebold, O. Guillon, M. Bram
Institut für Energie- und Klimaforschung
IEK-1: Werkstoffsynthese und Herstellungsverfahren
Forschungszentrum Jülich GmbH
Wilhelm-Johnen-Straße, 52428 Jülich, Germany
E-mail: m.bram@fz-juelich.de

F. Grosswendt, S. Weber
Institut für Werkstoffe
Lehrstuhl Werkstofftechnik
Ruhr-Universität Bochum
Universitätsstraße 150, 44801 Bochum, Germany

 The ORCID identification number(s) for the author(s) of this article can be found under <https://doi.org/10.1002/aesr.202300184>.

© 2023 The Authors. Advanced Energy and Sustainability Research published by Wiley-VCH GmbH. This is an open access article under the terms of the Creative Commons Attribution License, which permits use, distribution and reproduction in any medium, provided the original work is properly cited.

DOI: 10.1002/aesr.202300184

A.-C. Assmann
Institut für Anthropogene Stoffkreisläufe
ANTS
RWTH Aachen University
Wüllnerstr. 2, 52062 Aachen, Germany

M. Kregel
Magnetprototyping & Entwicklung Magnetische Werkstoffe
Wilo SE
Wilopark 1, 44263 Dortmund, Germany

F. Maccari, O. Gutfleisch
Institut für Materialwissenschaft
Funktionale Materialien
Technische Universität Darmstadt
Peter-Grünberg-Straße 16, 64287 Darmstadt, Germany

the potential to be harnessed as a valuable resource and recycled, which could mitigate the supply risk to an extent in the midterm.^[6] A variety of techniques are being explored for the extraction of REEs from e-waste, including pyrometallurgical, hydrometallurgical, solvent-based, and kinetics-based techniques.^[4,7–12] To minimize the use of potentially environmentally harmful acids or high energy for molten components, however, the direct recycling of Nd–Fe–B scrap particles without the need to break them down further into their constituent elements is an attractive alternative.

Nd–Fe–B magnets for industrial applications can be roughly divided into three types according to their preparation: sintered magnets, deformed magnets, and bonded magnets.

Fully dense magnets free from polymer binder, that therefore have higher Nd–Fe–B content, are the sintered and hot-deformed magnets. This higher Nd–Fe–B content leads to an exhibition of better magnetic properties. Sintered magnets are produced through a conventional powder metallurgy method, in which Nd–Fe–B single-crystal microcrystalline powders are magnetically aligned by applying a strong magnetic field when compacted into a green body, and freely sintered.^[13] Hot-deformed Nd–Fe–B magnets also start from nanocrystalline powders, but they are instead hot pressed and subsequently hot deformed or backextruded to obtain a fully dense magnet with a pronounced texture and anisotropic microstructure.^[14] Bonded magnets are formed from the combination of fine Nd–Fe–B powders with small crystallite size, typically prepared with melt spinning or hydrogenation–disproportionation–desorption–recombination (HDDR), with a polymer binder, such as epoxy.^[15,16] The mixture is compacted and cured to form the magnet. The focus of recycling of polymer-bonded magnets lies primarily in decomposition of the polymeric binder and liberation of the Nd–Fe–B powder.^[17,18]

Waste bulk Nd–Fe–B sintered magnets have become attractive as recycling candidates due to their high REE content (more than 30 wt%) and ability to maintain the physical and chemical properties of the original magnet within the bulk during their use phase, despite surface deterioration. Direct alloy techniques of recycling sintered magnets include resintering into a new magnet, melt spinning, HDDR, or recasting into a master alloy.^[19–22] In the case of resintering, unless additional Nd is blended in with the recycled powders, the magnetic properties decrease with each consecutive crushing and recycling of the powders. This is considered to be due to the oxidation of the grain boundary layer, causing it to no longer be able to melt during sintering and form Nd-rich grain boundary phase.^[23] Melt spinning, which involves the melting of Nd–Fe–B and casting onto a copper wheel to produce microstructurally amorphous/nanocrystalline flakes, has a high-power consumption due to the need to melt the material. It also has a loss of about 20–30 wt% of the magnet material.^[19,24] Hydrogen decrepitation (HD) occurs through the expansion of a material due to the absorption of hydrogen by exposing the material to hydrogen in a controlled atmosphere. However, after jet milling, this powder would be highly reactive and needs to be handled in an inert atmosphere.^[25] HDDR takes the hydrogen processing further by exposing Nd–Fe–B to hydrogen at temperatures around 750–900 °C, leading to the dissociation of the hard magnetic phase Nd₂Fe₁₄B into NdH₂, Fe₂B, and α-Fe. Reduction of the hydrogen pressure reverses the reaction to form submicrometer Nd₂Fe₁₄B grains enveloped in Nd-rich grain boundary

phase.^[26,27] All of these listed recycling options tend to require a lot of energy for melting or thermal treatments. This work seeks to explore a direct recycling technique that can avoid these additional costs or steps.

The crushing of sintered Nd–Fe–B magnets for recycling has been performed with the primary goal of producing anisotropic polymer bonded magnets.^[13,28,29] However, in a polymer bonded magnet, the remanence, which is the amount of magnetic induction that remains after magnetization, and energy product would be compromised relative to a sintered magnet, as binder volume, pore volume, and misorientation of the grains/powder.^[30–32]

To achieve the highest possible B_r , recycled magnets would have to be reformed into a fully dense sintered or hot-deformed magnet. As sintered magnets require microcrystalline starting material, the use of anisotropic scrap powder for recycled sintered magnets could potentially be a detriment, as thermomechanical grain alignment would not occur and excessive grain growth would decrease the coercivity, H_{cJ} .^[33,34] Hot deformation, however, remains an option for the recycling of anisotropic magnet scrap, but only if the scrap is nanocrystalline. Hot deformation occurs at around 800 °C to achieve the thermomechanical alignment of crystal grains and increases the aspect ratio of the grain size (lateral diameter of 200–500 nm, thickness of 20–50 nm), while simultaneously aligning the c-axis to the pressing direction. Prior to the hot deformation step, a hot pressing step is performed, which is presumed to melt the grain boundary phase (consisting primarily of Nd) and contribute to the anisotropic grain growth.^[34,35] Again, the use of nonideal anisotropic scrap Nd–Fe–B powder that is no longer nanocrystalline may also produce suboptimal results, as excessive grain growth may occur at this temperatures range.

Electric current-assisted sintering (ECAS) technologies have been explored for the production of anisotropic magnets. Electrodischarge sintering (EDS) has been shown to be a highly attractive ECAS method, due to its low-energy consumption relative to conventional sintering. However, it is limited in its ability to achieve anisotropic properties and varied part dimensions.^[36] A combination of field-assisted sintering techniques/spark plasma sintering (FAST/SPS) and flash SPS has been shown to generate new magnets from a 100% recycled Nd–Fe–B material feed, consisting of crushed powder made from hot-deformed Nd–Fe–B industrial scrap magnets.^[37] The magnetic powder was presintered using FAST/SPS into a pellet, and this pellet was deformed using flash SPS to induce anisotropic grain growth and alignment. The benefit of flash SPS when compared to conventional hot deformation is the simultaneous densification and deformation of the sample via a high-power current pulse, which has the potential of maintaining the nanoscale of the grains while producing the desired crystallographic texture.^[38] The investigations and optimizations of this process by Mishra et al. and Maccari et al. are the basis of this work.^[37,39]

Using parameters developed by Mishra et al.^[37] and Maccari et al.,^[39] this work aims to demonstrate the flash SPS deformation technique to produce well-performing magnets made from a varying weight percentage of crushed powder from scrap hot-deformed Nd–Fe–B magnets mixed with pristine commercial melt-spun Nd–Fe–B powder. The goal of this process is to improve the magnetic properties of the recycled magnets through the addition of varied amounts of pristine melt-spun

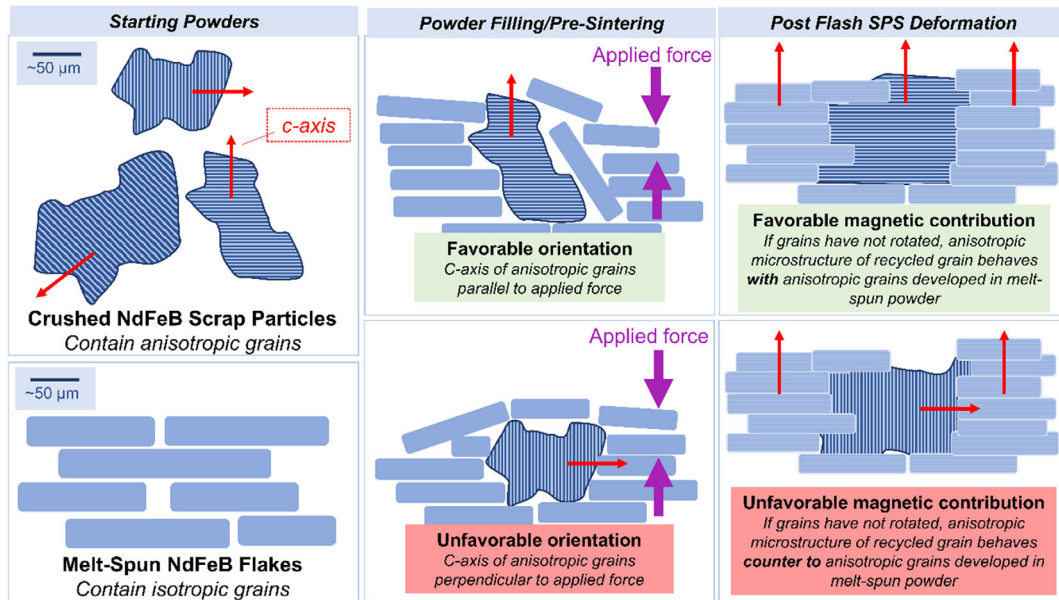


Figure 1. Possible effects of texture present in scrap Nd–Fe–B magnet powder on B_r , which decreases when there is large misalignment.

powder. Special care was taken to crush the scrap Nd–Fe–B magnets in a low-oxygen environment, as oxidation of Nd harms the Nd-rich phase needed for liquid-phase sintering and to magnetically decouple the $\text{Nd}_2\text{Fe}_{14}\text{B}$ grains.^[40,41] Textures already present in the scrap Nd–Fe–B grains, however, have the potential to be both an asset and a detriment, as schematically shown in **Figure 1**. If the ECAS process is not capable of forcing the texture of the anisotropic grains to rotate relative to the applied force, pockets of texture oriented in an opposing direction may decrease the magnetic performance. Therefore, granular deformation within the scrap powder and an anisotropic texturing of the melt-spun commercial powder (in the case of mixed scrap and commercial magnets) must happen simultaneously to achieve optimum magnetic properties.

As a point of reference, a commercial die-upset, hot-deformed magnet has H_{cJ} of 1342 kA m^{-1} , B_r of 1.30 T, and $(\text{BH})_{\text{max}}$ of 323 kJ m^{-3} . For industrial applications, the best compromise of remanence (magnetic stray field generated by the magnet) and coercivity (stability against demagnetization under opposing magnetic field) is aspired.^[37] Though it was not expected to reach this commercial target, as scrap hot-deformed magnet powder has the abovementioned restrictions compared to pristine melt-spun powders, and achieving properties close to commercial magnets is the ultimate goal of magnet recycling. Mishra et al. previously achieved a fully recycled magnet with a H_{cJ} of 809 kA m^{-1} and B_r of 1.10 T ($(\text{BH})_{\text{max}} = 189 \text{ kJ m}^{-3}$), and parameters used to generate this magnet were utilized in this study.^[37] The scope of this study focuses entirely on Nd–Fe–B scrap generated during industrial processes, that is, out-of-spec magnets created during magnet production. These magnets are not recovered from waste products and do not have any special treatment criteria outside of crushing into powder (e.g., cleaning of surface oxidation, cleaning of outside coatings, etc.)

2. Experimental Section

2.1. Starting Powders

Several magnetic powders were selected for processing, consisting of one commercial melt-spun powder (Magnequench MQU-F B55557) and four different recycle powders (produced from out-of-spec magnets from the company WILO SE). Magnequench MQU-F melt-spun powder (batch number B55557) was chosen as the base material. This is a commercially available melt-spun Nd–Fe–B powder with a ribbon-like morphology used as standard material for the production of anisotropic magnets via the hot deformation process. The ribbons contained nanocrystalline, isotropic grains of roughly 50 nm. Similar kinds of powder were used as the starting material for demonstrating alternative sintering technologies like FAST/SPS, flash SPS, and EDS as well.^[36,37,39,42,43] Utilization of this magnet powder allowed for the direct comparison of the effects of the FAST/SPS and flash SPS process between scrap magnet powder to pristine magnet powder.

Several streams of scrap magnet powder were processed. The first was powder provided by Less Common Metals (LCM Batch J9348/FP33302 delivered by WILO SE), referred to in this article as LCM1. This powder was produced through the crushing of out-of-spec Nd–Fe–B magnets provided by WILO. The powder contained particle sizes beneath $200 \mu\text{m}$, which was measured by both sieve analysis and laser diffraction particle size analysis. The crushing conditions for this magnetic material were not stated. This powder was considered to be reflective of a large-scale industrial Nd–Fe–B crushing process.

Three other scrap magnet powder streams were produced for experiments within this work. Crushing was done in a glovebox using a type BB 50 jaw crusher (Retsch GmbH, Haan, Germany) and the resulting powder was sieved to the desired particle size

range. Oxygen was controlled via the pumping of nitrogen filled in through the process. Due to imperfect sealing, a small amount of oxygen entered the chamber from the air, resulting in a residual oxygen content of 3 vol%. Three streams of crushed Nd–Fe–B were used in the experimental processes, referred to in this article as RC1, RC2, and RC3, respectively, and differing in their particle size range.

RC1 and RC2 were chosen to be closely related and therefore comparable to LCM1. This particle size range was chosen due to its relevancy to powder metallurgy (as opposed to RC3). RC1 was a mixture of particle size fractions below 200 μm . This included all the fractions <125 μm . RC1 was mixed with various particle size fractions to have a particle size distribution as close to LCM1 as possible. This was done in order to directly compare the effects of industrial processing with the lab-scale, oxygen-controlled processing of scrap magnets. RC2, however, focuses on a particle size range (125–250 μm). As shown in **Figure 2**, the much smaller particles (<125 μm) have a significant increase in oxygen content. Therefore, RC2 was selected in order to eliminate contamination present in the smaller particle size range.

Unlike RC2 and RC1, RC3 contained a particle size range of 500–1000 μm . This unusually large particle size range (from a powder metallurgical perspective) was selected due to two reasons. One, oxygen contamination analysis of the full sieved range of Nd–Fe–B crushed by RWTH Aachen showed that larger particles were less susceptible to oxygen contamination than smaller particles, with a significant increase in contamination in material below 200 μm (Figure 2). This contamination was associated with the increased specific surface area of smaller particles. Two, larger particles (>1000 μm) would likely not have worked in the FAST/SPS and flash SPS configuration. Therefore, special attention was paid to RC3 as this fraction could combine the low oxygen contamination with the upper limit of particle sizes that could be processed.

From these four different recycled powders, mixes of 5, 10, 15, 20, and 50 wt% recycled material were mixed with commercial

MQU-F. Pellets of these mixes were then precompacted and processed with FAST/SPS and flash SPS. Pellets of 100 wt% recycled material and 100 wt% commercial MQU-F were also processed for comparison.

2.2. Characterization of Magnet Powders

All powders were analyzed for particle size distribution using a Horiba LA-950V2 (Horiba Ltd., Japan) laser particle size analyzer with calculation via Fraunhofer theory. Nitrogen and oxygen contamination were analyzed using a NOH analyzer type TCH 600 (LECO Corporation, USA). The hysteresis loops of the magnetic powders were measured using a vibrating sample magnetometer (VSM) module in a physical property measurement system type VSM-PPMS14 (Quantum Design, USA). As the recycled powders were anisotropic, they were measured via VSM in both aligned and unaligned directions. This was done through setting the powders in a bicomponent epoxy glue and exposing them to a magnetic field as the epoxy cured. This caused the powder to rotate, due to the high magnetocrystalline energy of Nd–Fe–B, and aligned the c-axis of the powder particles along the magnetic field. MQU-F, an isotropic powder, was set in an epoxy without exposure to a magnetic field. Particle morphology and microstructures of the powders were analyzed via field-emission gun scanning electron microscopy (FEG–SEM, referred to in this work as SEM) using a Zeiss Gemini 450 (Carl Zeiss AG, Germany) using an acceleration voltage of 8 kV and working distance of 8.5 mm. A classical Everhardt–Thornley detector was used to image the morphology, and an InLens secondary electron (SE) detector was used for the microstructures. Inductively coupled plasma–optical emission spectroscopy (ICP–OES) was utilized for the determination of the powder composition using an iCAP 6500 ICP–OES CID Spectrometer (Thermo Fisher Scientific, USA).

2.3. FAST/SPS Presintering

15 g of magnet powder was precompacted into a graphite die (SGL Carbon, SIGRAFINE R7710) with an inner diameter of 20 mm. For tool preservation and improvement of sample contact, a graphite foil with thickness 0.35 mm (SGL Carbon, SIGRAFEX) was inserted. FAST/SPS was performed in an HP-D5 device (FCT Systeme GmbH, Rauenstein, Germany), and all experiments were performed under vacuum. The pellets were heated to a maximum temperature of 500 $^{\circ}\text{C}$ with a heating rate of 100 K min^{-1} and a dwell time at maximum temperature of 30 s. A constant pressure of 50 MPa (16 kN) was applied throughout the procedure. Relative density of the pellets ranged from 65% to 75%, and heights of the pellets were ≈ 8 mm. The pellets with the lowest densities (65–70%) were the pellets made from 100 wt% recycled material. FAST/SPS presintering was necessary for the generation of pellets with sufficient stability to withstand the force applied by H-HP-D 25 during the flash SPS deformation process. There is also evidence that suggests that presintering conditions influence the inhibition of grain growth in the flash SPS deformation step, as observed by Maccari et al.^[39]

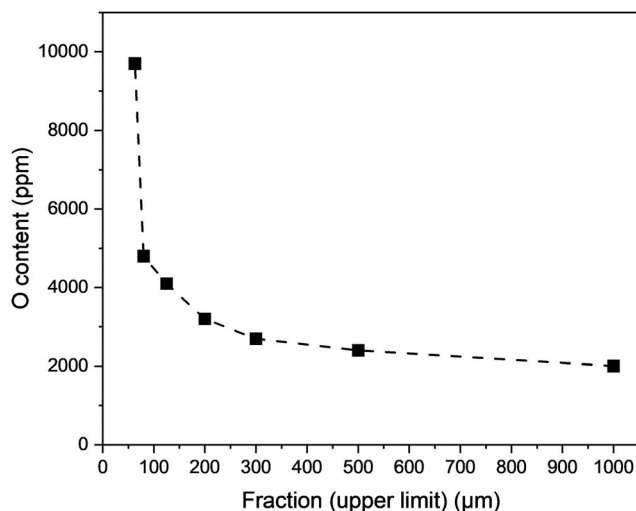


Figure 2. Oxygen contamination of crushed Nd–Fe–B powder for various particle sizes.

2.4. Flash SPS Deformation of Presintered Pellets

Flash SPS experiments were performed in a hybrid FAST/SPS device (H-HP-D 25 SD/FL/MoSi from FCT Systeme GmbH, Rauenstein, Germany). Flash SPS parameters were chosen based on the favorable results provided by Mishra et al.^[37] All Flash SPS experiments were done with presintered FAST/SPS pellets from the previous step. Experiments were performed under a vacuum of roughly 0.4 mbar. The presintered pellets were placed between two graphite punches (diameter 60 mm) with plane parallel surfaces. A load of 10 kN (roughly 32 MPa for a 20 mm sample) was applied to the samples. The samples were then preheated to 300 °C via direct Joule heating with a maximum heating power of 10 kW. The samples then dwelled at maximum temperature for 120 s. After dwell, the samples were subjected to a pulse of continuous direct current at a maximum power of 35 kW for a duration of 30 s. At the end of the power pulse, current was switched off to allow the sample to cool for 10 min before the vacuum was released and the chamber opened for sample extraction. The possibility of flash SPS processing with an outer die exists but was not performed during this work. The goal of this work was primarily to explore the limitations of adding scrap Nd–Fe–B powder to commercial powder and directly compare to the work of Mishra et al. and Maccari et al.^[37,39]

2.5. Characterization of Deformed Samples

Density of the FAST/SPS presintered samples was measured geometrically prior to deformation via flash SPS. Due to the deformed edges of the flash SPS samples, a 20 mm-diameter cut was made in the center of the deformed samples to extract the homogenous center for magnetic characterization and density measurements. Magnetic characterization was performed with Permagraph C-300 system (MAGNET-PHYSIK Dr. Steingroever GmbH, Köln, Germany) after previous

Table 1. ICP–OES compositional analysis of all Nd–Fe–B starting powders.

| Powder Name | Nd [wt%] | Fe [wt%] | B [wt%] | Ga [wt%] | Co [wt%] | Pr [wt%] |
|-------------|----------|----------|---------|----------|----------|----------|
| MQU-F | 30.6 | 60.0 | 0.80 | 0.54 | 5.57 | 0.11 |
| LCM1 | 30.0 | 59.0 | 0.81 | 0.55 | 5.28 | 0.13 |
| RC1 | 29.1 | 60.9 | 0.70 | 0.42 | 5.81 | 0.17 |
| RC2 | 30.2 | 63.1 | 0.75 | 0.45 | 6.00 | 0.20 |
| RC3 | 31.0 | 62.8 | 0.85 | 0.57 | 5.74 | 0.25 |

Table 2. Overview of magnetic powders and their properties, including aligned VSM measurements of magnetic properties.

| Powder Name | Origin | Processing | Particle Size Range [μm] | O content [ppm] | N content [ppm] | H_{cJ} [kA m ⁻¹] | B_r [T] | $(BH)_{max}$ [kJ m ⁻³] |
|-------------|--------------------------|-------------------------------|--------------------------|-----------------|-----------------|--------------------------------|-----------|------------------------------------|
| MQU-F | Magnequench B55557 | Melt-Spun | <400 | 1120 | 100 | 1693 | 0.74 | 90.5 |
| LCM1 | WILO out-of-spec magnets | Crushed by Less Common Metals | <200 | 6060 | 1000 | 1312 | 1.06 | 179.0 |
| RC1 | WILO out-of-spec magnets | Crushed by RWTH Aachen | <200 | 6000 | 350 | 1097 | 1.22 | 225.6 |
| RC2 | WILO out-of-spec magnets | Crushed by RWTH Aachen | 200–125 | 2500 | 80 | 1140 | 1.28 | 284.3 |
| RC3 | WILO out-of-spec magnets | Crushed by RWTH Aachen | 500–1000 | 2350 | 230 | 1174 | 1.31 | 315.6 |

magnetization in a pulsed field. Density measurements were performed using the Archimedes principle. All density measurements were compared to a theoretical density of 7.55 g cm⁻³. For microstructural characterization, SEM was conducted with FEG-SEM JEOL JSM-7600 (JEOL, Japan) operated in the SE mode with a working distance of 8 mm and an acceleration voltage of 15.0 kV. Energy-dispersive X-Ray analysis (EDX) was performed with an Oxford Instruments X-Max 80 mm² detector (Oxford Instruments, UK). Prior to SEM analysis, samples were embedded in a nonconductive epoxy resin and ground to 1200 grit. Subsequently, samples were polished with 6, 3, and 1 μm diamond paste and a water-free SiO₂ suspension.

3. Results and Discussion

3.1. Properties of the Different Starting Powders

Table 1 provides the composition of all Nd–Fe–B powders used in these experiments. As shown in this table, Ga, Co, and Pr were added as a means to improve magnetic properties. Both the MQU-F melt-spun powder and the recycle materials contain similar amounts of each alloying element.

Table 2 summarizes the interstitial contents and the magnetic properties of all powders. LCM1 has the highest oxygen contamination of all recycled powders (6060 ppm) and the lowest B_r in the aligned VSM measurements (1.06 T). As the scrap magnets were already hot-deformed prior to crushing; all recycled powders in this study still maintain anisotropy from the initial magnet forming process. This can be seen in their flattened grain shape in **Figure 3**. Therefore, magnetic properties differ when measured in aligned or unaligned orientations. Also of note is the grain size of RC1, RC2, and RC3: most grains have a lateral diameter below 500 nm and a visually high width-to-height ratio. This would ideally be maintained during the combination of FAST/SPS presintering and flash SPS deformation. Of note, RC3 has the highest B_r and H_{cJ} of all scrap material when measured in the aligned direction (Table 2). This is in disagreement with the measurements of Li et al. who accomplished their most optimized magnetic properties with regenerated crushed powders of particle size 200–450 μm.^[28] It is possible that their additional annealing step at 1073 K for 1 h caused grain growth, leading to a decrease in H_{cJ} .

Despite being considerably smaller than RC3, RC2 still has a B_r still has a comparable H_{cJ} and B_r (1140 kA m⁻¹ and 1.28 T). RC1 has the lowest B_r and H_{cJ} (1.22 T and 1097 kA m⁻¹) of all (1.22 T and 1097 kA m⁻¹) of all the powders crushed by RWTH Aachen, yet has a higher B_r than LCM1, despite being designed

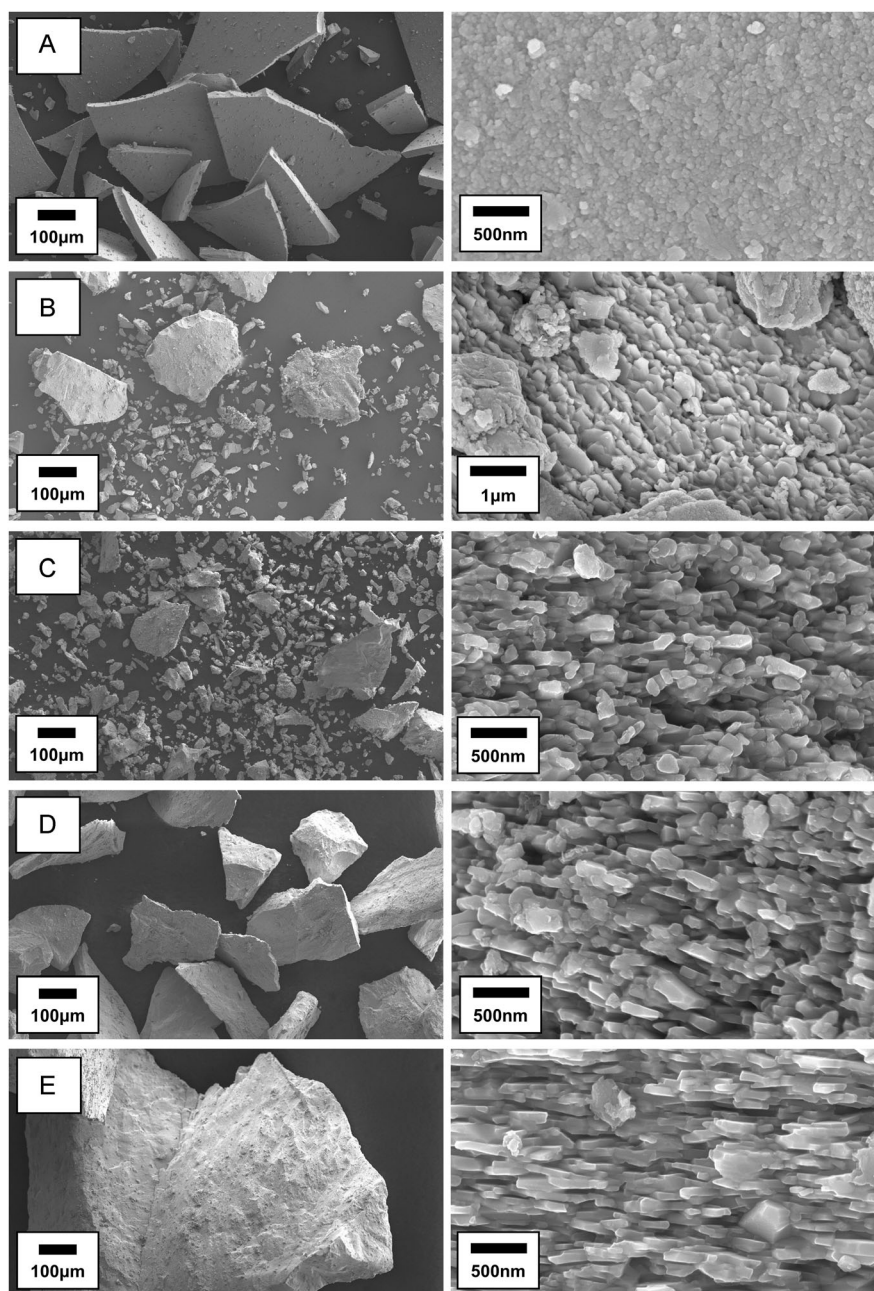


Figure 3. SEM (SE detector) images of A) MQU-F, B) LCM1, C) RC1, D) RC2, and E) RC3 displaying differences in particle morphology (left) and grain size plus anisotropy (right).

to be as similar to LCM1 as possible. The cause for this is likely not oxygen contamination, as the two powders have a very similar amount of measured oxygen content (LCM1: 6060 ppm, RC1: 6000 ppm). LCM1 does have a significantly higher amount of nitrogen, however, which could be responsible for hindering the magnetic properties, perhaps through the formation of nitrides.^[44]

The wide difference in the morphology and size of the powders can be seen in Figure 3. The flat, platelet shape of the

MQU-F powder contrasts greatly with the blocky, irregular shapes of the crushed magnets. The elimination of small particles and increase in size from RC1 to RC2 to RC3 are also visible, with RC3 particles so large that only 1–2 particles can be seen at the same magnification as all other powders, which have tens to hundreds of particles visible in an image. As RC3 has much larger particle size, fracture surfaces with identifiable grain structures were more available to be imaged. RC1 and RC2, due to their smaller particle size, provided

limited fracture surfaces oriented in the correct way for the grain structure to be imaged via SEM. This is a possible explanation for discrepancies in imaged grain alignment and orientation. However, it is also important to note that as this material was processed from scrap, discrepancies in microstructure and composition may exist as is the case in the present work.

3.2. Properties of FAST/SPS Presintered and Flash SPS Deformed Samples

For direct comparison of properties of other magnet types to the flash SPS magnets made from scrap magnet material, **Table 3** is provided as a reference. This reference includes work by Mishra et al. in the flash SPS processing of 100 wt% LCM scrap Nd-Fe-B powder, of which the same batch was used in this work.^[37] The properties listed represent the sample processed with the same FAST/SPS and flash SPS processing parameters used in this work. Ideally, the best compromise of H_{cJ} and B_r would be achieved to develop as high of $(BH)_{max}$ as possible. On the other hand, achieving higher $(BH)_{max}$ often increases processing costs. As a consequence, a wide variety of magnet grades of varied B_r and H_{cJ} values exist commercially for a wide range of applications.^[45]

Figure 4 and **Table 4** display the magnetic properties of the flash SPS deformed samples. The MQU-F reference sample had the highest values across all magnetic properties ($H_{cJ} = 1587 \text{ kA m}^{-1}$, $B_r = 1.13 \text{ T}$, $(BH)_{max} = 243 \text{ kJ m}^{-3}$). This is close to and in agreement with the results of Mishra et al. for the same parameters ($H_{cJ} = 1483 \text{ kA m}^{-1}$, $B_r = 1.18 \text{ T}$, $(BH)_{max} = 264 \text{ kJ m}^{-3}$) with likely some variation in density causing the differences in B_r .^[37] Further improvement to these properties by fine tuning the parameters has been performed by Maccari et al.^[39] but these results were received too late for consideration in this work. Flash SPS deformation led to an increase in density in pellets ranging from 89 to 99% relative density.

The sample made from 100 wt% LCM1 ($H_{cJ} = 724 \text{ kA m}^{-1}$, $B_r = 1.1 \text{ T}$, $(BH)_{max} = 171 \text{ kJ m}^{-3}$) has properties similar to the sample made from Mishra et al. with the same flash SPS parameter ($H_{cJ} = 809 \text{ kA m}^{-1}$, $B_r = 1.1 \text{ T}$, $(BH)_{max} = 189 \text{ kJ m}^{-3}$). Similar B_r values are seen across decreasing wt% of LCM1 powder, with a maximum of 1.11–1.12 T from 5 to 15 wt% LCM1. H_{cJ} of magnets containing LCM1 hover around 1500 kA m^{-1} until

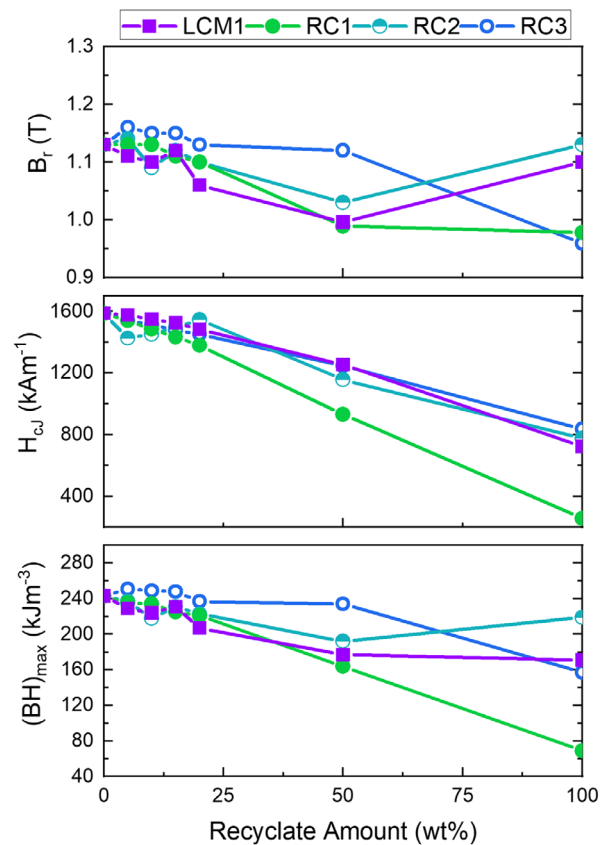


Figure 4. B_r , H_{cJ} , and $(BH)_{max}$ of flash SPS samples containing varied amounts of recycled material.

20 wt% LCM1 is surpassed. The peak of H_{cJ} ($H_{cJ} = 1549 \text{ kA m}^{-1}$) occurs at 10 wt% LCM1, while peak $(BH)_{max}$ (231 kJ m^{-3}) for the LCM1 mix is at 15 wt% LCM1. Between 10 and 15 wt% may be the point at which enough recycled material (which has already been deformed and therefore already has grain anisotropy and alignment) contributes positively to the magnetic properties of the sample. H_{cJ} decreases rather linearly with increased amount of LCM1.

RC1, which was mixed to be similar to LCM1, had a lower B_r than LCM1 at 100 wt% ($B_r = 0.96 \text{ T}$) and the lowest H_{cJ} and

Table 3. Coercivity H_{cJ} in kA m^{-1} , remanence B_r in T, and energy product $(BH)_{max}$ in kJ m^{-3} of differently processed Nd-Fe-B magnets, including an example of polymer-bonded magnets made from recycled sintered Nd-Fe-B magnets.

| Process | Coercivity H_{cJ} in $[\text{kA m}^{-1}]$ | Remanence B_r in [T] | Energy Product $(BH)_{max}$ in $[\text{kJ m}^{-3}]$ |
|---|---|------------------------|---|
| EDS ^[36,42] | 1565 | 0.78 | 102 |
| Hot-Pressing ^[37] | 1569 | 0.83 | 120 |
| FAST/SPS ^[37] | 1683 | 0.84 | 123 |
| Die-Upsetting ^[37] | 1342 | 1.30 | 323 |
| Flash SPS (MQU-F) ^[37] | 1483 | 1.18 | 264 |
| Flash SPS (LCM scrap Nd-Fe-B powder) ^[37] | 809 | 1.10 | 189 |
| Polymer Bonded (commercial, MQ1-12, Magnequench) ^[55] | 675–800 | 0.74–0.80 | 92–99 |
| Polymer Bonded (Nd-Fe-B powder from scrap sintered magnets) ^[28] | 940 | 0.838 | 91.4 |

Table 4. Properties of starting powders, FAST/SPS presintered pellets, and flash SPS deformed pellets.

| Starting Powder | | | | | Pre-Sintered State | | Deformed State | | | | | |
|-----------------|--------------------|----------------|--------------------------------------|------------------|--------------------|----------------------|--------------------|--------------------------------|----------------------|--------------------------------|-----------|------------------------------------|
| Sample Code | Melt-spun Material | Scrap Material | Particle size range [recyclate] [μm] | wt% of Recyclate | Sample height [mm] | Relative density [%] | Sample height [mm] | Deform. Degree z-direction [%] | Relative density [%] | H_{cJ} [kA m ⁻¹] | B_r [T] | $(BH)_{max}$ [kJ m ⁻³] |
| MQU-F | MQU-F | none | N/A | 0 | 7.4 | 80 | 3.09 | 58 | 96 | 1587 | 1.13 | 243 |
| LCM1-9505 | MQU-F | LCM1 | <200 | 5 | 7.55 | 78 | 3.53 | 53 | 97 | 1576 | 1.11 | 229 |
| LCM1-9010 | MQU-F | LCM1 | <200 | 10 | 7.92 | 75 | 3.32 | 58 | 96 | 1549 | 1.10 | 224 |
| LCM1-8515 | MQU-F | LCM1 | <200 | 15 | 8.04 | 73 | 3.52 | 56 | 96 | 1525 | 1.12 | 231 |
| LCM1-8020 | MQU-F | LCM1 | <200 | 20 | 7.82 | 75 | 3.47 | 56 | 94 | 1482 | 1.06 | 207 |
| LCM1-5050 | MQU-F | LCM1 | <200 | 50 | 8.15 | 72 | 3.70 | 55 | 97 | 1255 | 1.00 | 177 |
| LCM1-0100 | MQU-F | LCM1 | <200 | 100 | 8.4 | 70 | 3.68 | 56 | 95 | 724 | 1.10 | 171 |
| RC1-9505 | MQU-F | RC1 | <200 | 5 | 7.87 | 75 | 3.33 | 58 | 99 | 1540 | 1.13 | 235 |
| RC1-9010 | MQU-F | RC1 | <200 | 10 | 7.75 | 74 | 3.34 | 57 | 98 | 1485 | 1.13 | 234 |
| RC1-8515 | MQU-F | RC1 | <200 | 15 | 7.9 | 75 | 3.39 | 57 | 97 | 1433 | 1.11 | 225 |
| RC1-8020 | MQU-F | RC1 | <200 | 20 | 7.56 | 74 | 3.39 | 55 | 93 | 1379 | 1.10 | 221 |
| RC1-5050 | MQU-F | RC1 | <200 | 50 | 8.11 | 72 | 3.31 | 59 | 98 | 931 | 0.99 | 931 |
| RC1-0100 | MQU-F | RC1 | <200 | 100 | 8.95 | 65 | 4.06 | 55 | 96 | 257 | 0.98 | 69 |
| RC2-9505 | MQU-F | RC2 | 125–200 | 5 | 7.74 | 75 | 3.43 | 56 | 96 | 1426 | 1.14 | 237 |
| RC2-9010 | MQU-F | RC2 | 125–200 | 10 | 7.77 | 74 | 3.47 | 55 | 98 | 1452 | 1.09 | 218 |
| RC2-8515 | MQU-F | RC2 | 125–200 | 15 | 7.66 | 75 | 3.46 | 55 | 97 | 1497 | 1.12 | 231 |
| RC2-8020 | MQU-F | RC2 | 125–200 | 20 | 7.87 | 74 | 3.49 | 56 | 97 | 1546 | 1.10 | 223 |
| RC2-5050 | MQU-F | RC2 | 125–200 | 50 | 8.1 | 72 | 3.67 | 55 | 98 | 1156 | 1.03 | 192 |
| RC2-0100 | MQU-F | RC2 | 125–200 | 100 | 8.3 | 70 | 3.31 | 60 | 95 | 776 | 1.13 | 219 |
| RC3-9505 | MQU-F | RC3 | 500–1000 | 5 | 7.61 | 77 | 3.30 | 57 | 95 | 1544 | 1.16 | 251 |
| RC3-9010 | MQU-F | RC3 | 500–1000 | 10 | 7.88 | 74 | 3.27 | 59 | 92 | 1513 | 1.15 | 249 |
| RC3-8515 | MQU-F | RC3 | 500–1000 | 15 | 7.66 | 77 | 3.27 | 57 | 93 | 1479 | 1.15 | 248 |
| RC3-8020 | MQU-F | RC3 | 500–1000 | 20 | 7.65 | 77 | 3.06 | 60 | 98 | 1452 | 1.13 | 237 |
| RC3-5050 | MQU-F | RC3 | 500–1000 | 50 | 7.85 | 73 | 3.31 | 58 | 95 | 1247 | 1.12 | 234 |
| RC3-0100 | MQU-F | RC3 | 500–1000 | 100 | 8.34 | 71 | 2.72 | 67 | 89 | 836 | 0.96 | 157 |

$(BH)_{max}$ of all 100 wt% recycled samples. Similar to LCM1, H_{cJ} values consistently decrease with increasing wt% of RC1. Mixes of RC2, similar to LCM1, maintain consistent B_r values, even when approaching 100 wt% recycled material. 100 wt% RC2 is the only fully recyclate sample to have a B_r above 1.1 T. H_{cJ} values of RC2 mix surpass 1400 kA m⁻¹, even at 20 wt% RC2, as opposed to RC1, which sees a larger dip in H_{cJ} at 20 wt%. The removal of the fine powder fraction, when comparing RC2 to RC1, clearly has a positive effect on the magnetic properties.

In terms of magnetic properties, samples made from a mix of RC3 outperformed all other samples in B_r , with samples of up to 20 wt% RC3 reaching nearly 1.15 T. However, remanence decreases abruptly beyond 50 wt% RC3, likely due to the drop in density.^[46] Much like the samples produced by Mishra et al.,^[37] the deformed samples after flash SPS tended to have ragged, cracked edges and a more homogeneous center. This effect was also much more pronounced with the 100 wt% RC3 sample, as shown in **Figure 5**. The edges of this sample were mechanically unstable and would crumble to the touch.

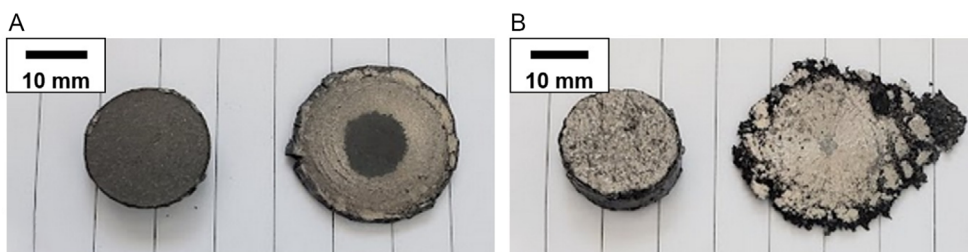


Figure 5. Comparison of FAST/SPS presintered pellets with flash SPS hot-deformed pellets for A) 100% LCM1 and B) 100% RC3.

Likewise, the sample with the lowest density was the sample made from 100 wt% RC3. This is likely due to the fact that this sample consisted entirely of large particles that were subjected to hot deformation and were already fully dense and therefore more resistant to second deformation. The particle size range of 500–1000 μm also did not permit for small particles to fill in the gaps created by the larger particles. Shifting the particle size range to include smaller particles, as those in the 200–500 μm range, may improve the density.

When comparing the results of all magnetic properties, the highest wt% mix of scrap with the best properties was 50 wt% RC3 ($H_{cJ} = 1247 \text{ kA m}^{-1}$, $B_r = 1.12 \text{ T}$, $(BH)_{\text{max}} = 234 \text{ kJ m}^{-3}$). However, the large particle size of the scrap material leads to high brittleness after deformation. This sort of brittleness may not be optimal for net shaping of recycled magnets, which will be a large aspect of our future work.

When considering a magnet made from 100 wt% recycled material, RC2 is preferred. This powder fraction leads to the best compromise of deformability and magnetic properties. As shown in Figure 5, 100 wt% LCM1 powder leads to a much more homogenous and stable pellet. RC2, being very similar to

LCM1, behaves similarly and would be easier to deform than RC3. Notable, though, is that RC2 only barely outperforms LCM1 in mixes from 5 to 50 wt%. Therefore, LCM1 could still be considered a viable recyclate option. During the crushing process of hot-deformed scrap magnets, it is difficult to avoid the formation of fine powder fractions, given the brittleness of the material. However, the fine fraction can be easily removed by sieving, leaving more desirable, large powder fractions for processing. Unfortunately, this creates a waste stream of fine powder, which, due to its high oxygen affinity, is difficult to use in another direct recycling process. Potentially, a waste stream like this could be recycled with a different technique, such as remelting.

3.3. Microstructure Through Different Processing Stages

Figure 6 shows several SEM images for FAST/SPS presintered and flash SPS deformed samples made from 100 wt% commercial and scrap material. In comparison, Figure 7 provides SEM images of samples with 15 wt% of recyclates LCM1 and RC3. Arrows in the upper-right corner of each image show the

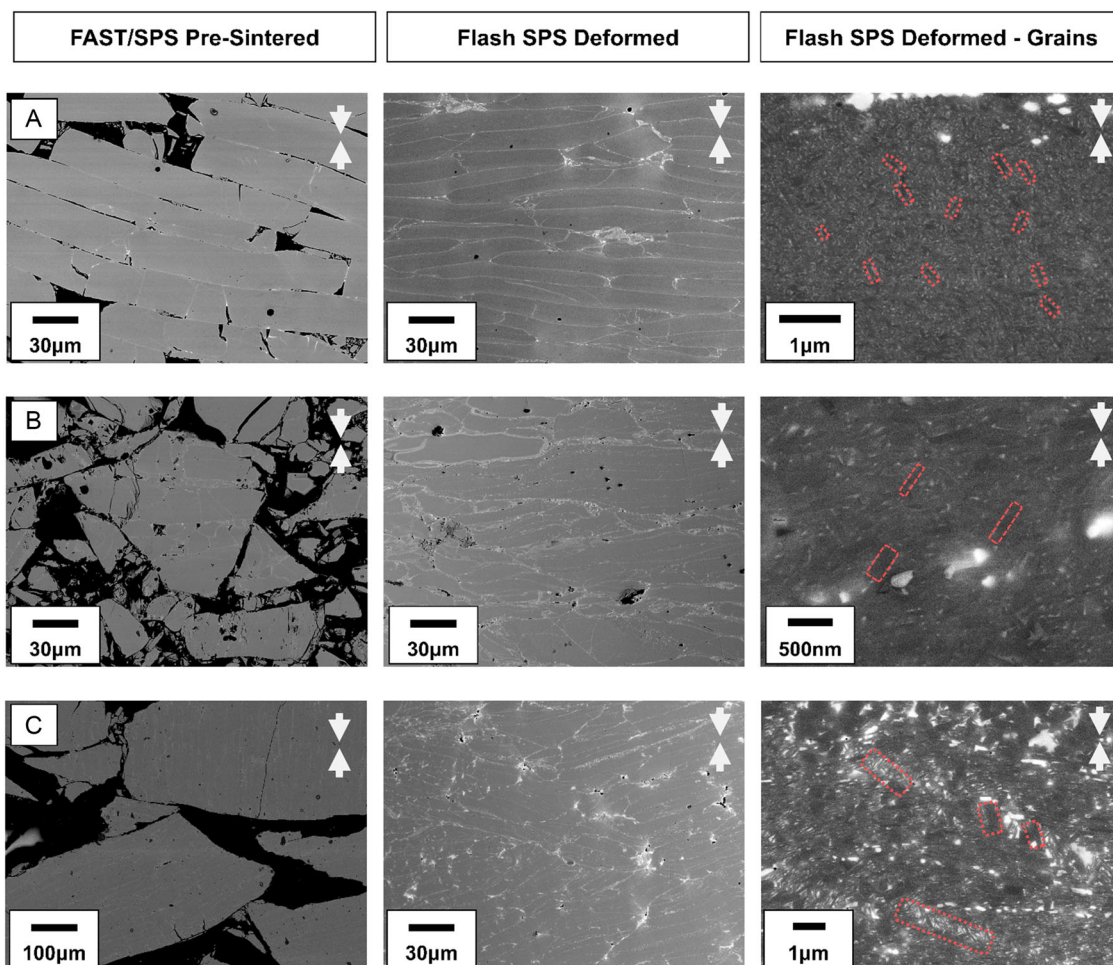


Figure 6. SEM (backscatter detector) images of the FAST/SPS presintered morphology, flash SPS deformed morphology, and granular microstructure of A) 100 wt% MQU-F sample, B) 100 wt% LCM sample, and C) 100 wt% RC3 sample. Contrast has been enhanced for grain visibility. Examples of unaligned grains are highlighted in red.

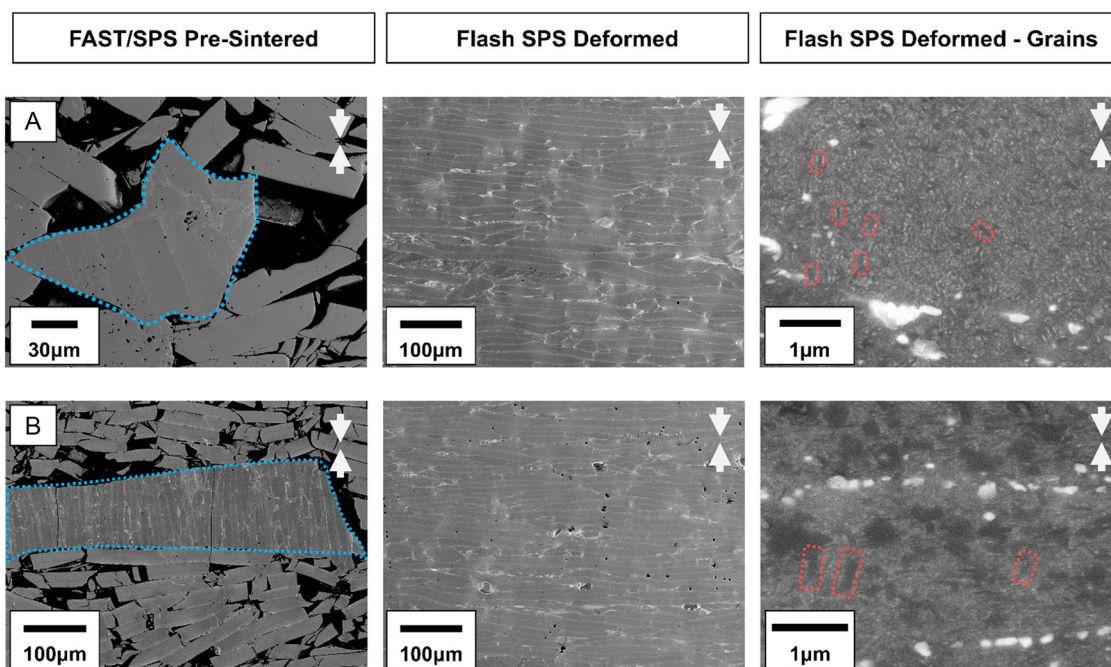


Figure 7. SEM (backscatter detector) images of the FAST/SPS presintered morphology, flash SPS deformed morphology, and granular microstructure of A) 15 wt% LCM1 sample and B) 15 wt% RC3 sample. Contrast has been enhanced for grain visibility. Examples of unaligned grains are highlighted in red. Recylate particles are highlighted in blue.

direction of applied force in both the FAST/SPS presintering and flash SPS deformation stages. The presintered stage shows large porosity within the samples. This feature is what allows for the direct production of new magnets via 100 wt% scrap material through flash SPS deformation. In the industrial scale of hot deformation process, samples must be near completely dense by hot pressing prior to hot deformation. Industrially, the hot-pressing step is performed at temperatures much higher than 500 °C used in the FAST/SPS presintering. This hot-pressing step leads to accelerated grain growth, making it an unattractive option for the direct recycling of anisotropic scrap magnet powder through redeformation.

As shown in the presintered stage for samples containing any amount of recycled material, the particles of recylate are distinct in size and shape to the melt-spun flakes of pristine MQU-F. MQU-F can be seen wrapped around the abnormal shapes of the recycled particles, some flakes even are cracked or broken from conforming to the shapes of the recycled particles. Excess cracking and wide variations in particle size create more powder particle contact points, which in turn are expected to lead to higher heat generation during flash SPS, according to the Joule heating effect.^[37] The higher heat generation from the transition points may lead to the easier melting of the Nd-rich particles during the deformation process. As shown in the deformed 100 wt% LCM1 and 100 wt% RC3 samples, bright regions (which correspond to Nd-rich phase concentration) are much more frequent and pronounced when compared to samples containing high amounts of pristine MQU-F. This could be due to coarsening of already existing grain boundaries from the previous deformation of the recylate particles, combined with high heat generated from a higher number of cracks and particle interfaces

generating segregation of the Nd-rich liquid phase in the process.^[41,47] Localized heating at cracks occurs due to the change of direction of the electric current at the tips of the crack, causing heat concentrations at the crack tips.^[48,49] A high number of cracks in the sample during the flash SPS phase could lead to many localized hotspots with a higher rate of Nd-rich phase melting, potentially creating higher concentrations of this phase throughout the sample. Formation of an especially thick Nd-rich region is often associated with contaminants, such as oxygen, on the particle surface and Nd surface segregation.^[35] A high segregation of Nd could be one of the reasons of the drop in H_{c1} seen in all-high-recylate percent samples in Figure 4, as in an ideal case, the Nd-rich phase would surround the $Nd_2Fe_{14}B$ grains, decreasing the magnetic coupling and improving the coercivity.

Coarsening of the nanocrystalline grains is another reason for the drop of H_{c1} . This effect occurs in all samples during the deformation stage, but the most notable occurs at interfaces and within what is suspected to be previously recycled particles. In Figure 7, SEM analysis shows that the integration of recycled particles into the matrix is relatively homogeneous. Recylate particles, highlighted in the presintered stage with a blue outline, cannot be differentiated in the deformed matrix anymore. Therefore, in mixed recycled/commercial samples, attributing certain features in the flash SPS microstructure to either the MQU-F or recylate powder is not always accurate.

The deformation stage with flash SPS is seen to promote anisotropic grain growth and texture in the samples. In Figure 6, the final stage 100 wt% MQU-F sample appears to have rectangular grains of <500 nm, even though they are not very well aligned. In Figure 7, 85 wt% MQU-F and 15 wt% RC3 have instances of blocky, square-shaped grains. Though differentiation between

recycled powder and commercial powder is not quite possible in the flash SPS SEM images, it can be inferred that the larger grains originate from the isotropic growth of grains in the originally hot-deformed recycle powder. This inference is made due to the 100 wt% MQU-F sample not displaying similar grain growth.

Unlike Mishra et al., texturing of Nd–Fe–B was not performed successfully at the nanocrystalline level. In both Figure 6 and 7, grains with a high degree of unalignment are highlighted in red. Ideally, the grains would have elongated morphology and stacked in a brick-wall-like structure perpendicular to the applied force. However, this was not observed. In Figure 6C, the case of the 100 wt% RC3 sample, some alignment can be seen. This alignment likely came from the initial hot deformation of the magnet, as the alignment is not perpendicular to the pressing direction and is isolated to the observed particle. This lack of texture is part of what drives the low B_r observed in nearly all samples. Improvement to texturing would lead to an improvement in B_r and consequently on the energy product.

The relatively high B_r seen in RC3 samples is expected to be due to the large particles creating islands of alignment within the bulk of the magnet sample. In contrast, these islands may also be counterproductive to B_r , as the particles are randomly oriented in the bulk, as schematically shown in Figure 1. An example of this can be seen in Figure 7B, in the FAST/SPS presintered column. A large RC3 particle (outlined in blue) shows particle texture from its first hot deformation. Though this is not a view of the granular structure; it can be assumed that, due to the nature of the hot deformation process, the orientation of the grains is similar to that of the particles. These particles are columnar, with their long, lateral sides parallel to the pressing direction. Unless the pressing force during deformation is large enough to promote full 90° rotation of the grains within the particles, to force the c-axis perpendicular to the pressing direction, the magnet will not achieve the highest possible remanence.^[34]

Unaligned islands detract from B_r , decreasing the performance of the magnet, as seen in the large gap between aligned and unaligned B_r of the powders in Table 2. Literature suggests that stress needed to die-upset Nd–Fe–B by 50% is roughly ≈69 MPa at 730 °C, which is very close to the maximum temperature achieved during the flash phase of the flash SPS process.^[35] Increase of the applied pressure during the flash phase may lead to better grain alignment and will be another focus of our ongoing experiments.

A less common occurrence, though still observed, was the presence of the secondary phase, likely $\text{Nd}_6(\text{Fe},\text{Co})_{13}\text{Ga}$. This phase was observed in the 100% RC3 sample and analyzed via EDX, as shown in Figure 8 and Table 5. Though the observance of this phase was extremely infrequent (only observed in two samples), the presence of any secondary phase detracting from the bulk magnetic properties as $\text{Nd}_6(\text{Fe},\text{Co})_{13}\text{Ga}$ is antiferromagnetic.^[50–54]

3.4. Influence of Oxygen Contamination on Magnetic Properties

One key aspect of this work was the comparison on Nd–Fe–B magnets crushed in a controlled (3 vol%) O_2 environment (RC1, RC2, RC3) compared to Nd–Fe–B magnets crushed in

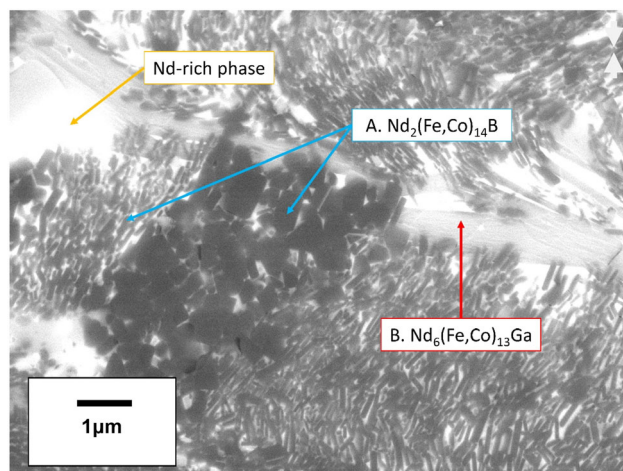


Figure 8. FEG-SEM of 100 wt% RC3 after flash SPS deformation showing EDX point data indicating a likely $\text{Nd}_6(\text{Fe},\text{Co})_{13}\text{Ga}$ phase (red). Fine and coarse $\text{Nd}_2\text{Fe}_{14}\text{B}$ phases can also be seen in this image.

Table 5. Elements analyzed via EDX of the point spectrums of a and B corresponding to Figure 8.

| Spectrum | Fe | Co | Ga | Nd |
|----------|-------|------|------|-------|
| A | 57.02 | 7.37 | 7.76 | 27.85 |
| B | 78.54 | 7.75 | – | 13.71 |

an industrial environment (LCM1). As shown in Figure 2, even in a controlled oxygen environment, the oxygen content increases greatly in Nd–Fe–B particles beneath ≈100–200 μm. Therefore, any volume of particles <100 μm had an effect on the final magnetic properties, most notably on H_{cJ} . Figure 9 displays the relationships between particle size and oxygen content in starting powders, along with the final H_{cJ} measured from flash SPS deformed samples made from 100 wt% of each powder.

LCM1 and RC1 show the highest oxygen content, at >6000 ppm for each (Table 2). This is reflected in their respective flash SPS samples having the lowest H_{cJ} among all samples. However, 100 wt% RC1 has a considerably lower H_{cJ} (257 kA m⁻¹) despite having a comparable oxygen contamination (6000 ppm for RC1, 6060 ppm for LCM1). RC1 was mixed to be as similar to LCM1 as possible. In Figure 10, though, the particle size distribution of RC1 shows a much higher frequency of very small (10–50 μm) particles. It was assumed that a greater fine powder fraction would lead to higher oxygen contamination, but this does not seem to be the case, as LCM1 and RC1 have very similar contamination levels. This may be due to RC1 being processed in a more oxygen-controlled environment (3 vol% O_2).

Oxygen contamination may not be the only contributor to a very low H_{cJ} . As shown in Figure 6, in the LCM1 images, the presence of more small particles, therefore, more contact points, contributes to greater Nd segregation and therefore poorer distribution of the Nd-rich phase. This is likely due to Joule heating at the many interfaces between smaller particles and cracks within the particles, alongside the higher Nd content at the surface of the particles.^[35,47] Poor distribution of the Nd-rich phase

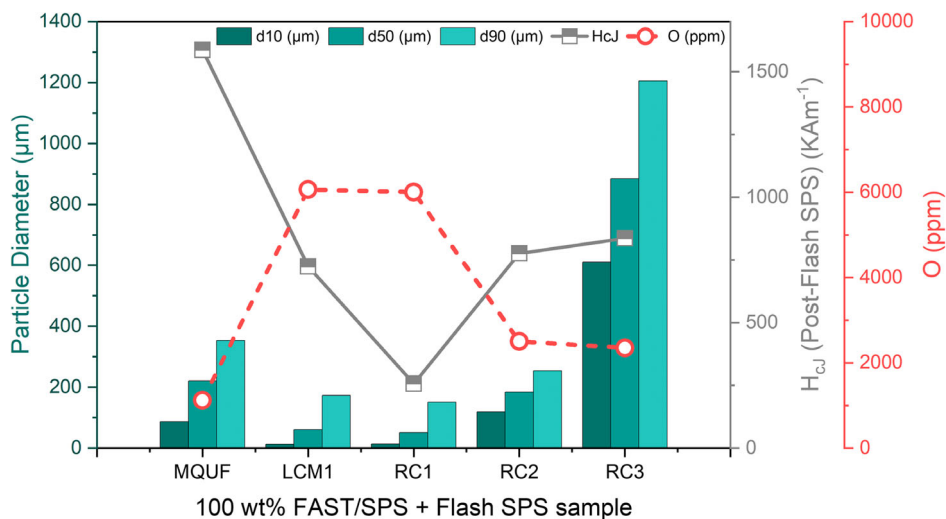


Figure 9. Comparison of particle sizes (d10, d50, and d90) (blue) and oxygen contamination of starting powders (red) with H_{c_j} (grey) measured from FAST/SPS presintered and flash SPS deformed samples made from 100 wt% of each powder.

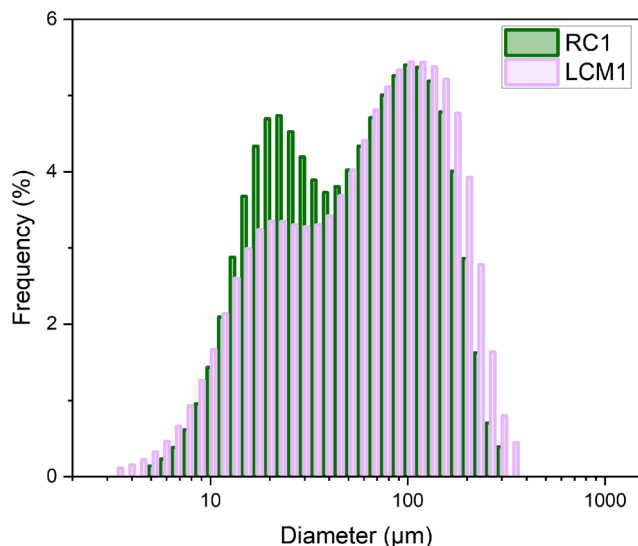


Figure 10. Particle size distribution difference between RC1 (green) and LCM1 (purple).

means that $\text{Nd}_2\text{Fe}_{14}\text{B}$ grains can be in contact and magnetically coupled, which is detrimental to coercivity. Also, as smaller particle sizes lead to more interfaces, and interfaces generate more heat during the flash SPS process, grain growth along interfaces could be more pronounced, also diminishing coercivity.

In contrast, 100 wt% LCM1, RC3, and RC2 all maintained similar H_{c_j} (724, 836, and 776 kA m^{-1} , respectively). While RC3 was expected to outperform LCM1 and RC2 significantly, due to it having much lower oxygen contamination, it ultimately behaved similarly and faltered in B_r due to its subpar densification. The primary difference between RC1 and RC2 is the elimination (or inclusion) of Nd-Fe-B particles $<125 \mu\text{m}$. Eliminating powders $<125 \mu\text{m}$ from a batch of crushed Nd-Fe-B led to a near-3 times increase in H_{c_j} and a 15% increase in B_r . Likely magnetic

properties of LCM1 could be improved through the sieving out of material $<125 \mu\text{m}$. However, that would lead to a large volume of discarded powder, as LCM1's d50 is below $100 \mu\text{m}$.

4. Conclusion and Outlook

In the context of circular economy, end-of-life or out-of-spec Nd-Fe-B hot-deformed magnets have become attractive recycling candidates due to their high amounts of REEs. Among other direct alloy technologies for recycling of Nd-Fe-B magnets, we have shown that is possible to generate magnets from scrap material mixed with commercial Nd-Fe-B melt-spun flakes. Flash SPS-formed magnets with 20 wt% of recycled material were capable of reaching H_{c_j} above 1300 kA m^{-1} and $(\text{BH})_{\text{max}}$ of over 200 kJ m^{-3} . Even magnets made of 100 wt% recycled material still showed anisotropic properties though they were at the expense of H_{c_j} . Detailed microstructural analysis did not show the desired pronounced texture, but anisotropic grain growth was still achieved, exhibiting the possibility for further optimization and texture development, for example, through the increase of pressure during hot deformation. The particle size of the magnet scrap had a distinct influence on the resulting properties. The use of Nd-Fe-B particle fractions that were too small ($<125 \mu\text{m}$) both introduced more oxygen contamination into the system due to the higher specific surface and produced excessive Nd-rich segregated regions. The resulting magnetic properties in samples made from scrap material are not competitive with in-spec, commercial, anisotropic hot-deformed magnets. Nevertheless, magnets with clearly pronounced anisotropic properties were produced, which is not the case for other scrap recycling techniques such as polymer bonding or EDS.

The optimization of flash SPS parameters for the deformation of recycled Nd-Fe-B material is still ongoing for the fine tuning of the microstructure. Improving textures during the deformation step would further improve the B_r of the final magnets. This technology is suitable for planar-shaped magnets, but less

so for ring-shaped magnets. Modifying the process for the net shaping of these magnetic powders into their final shape, with a large diameter-to-height ratio, is also of utmost priority. However, the results presented in this work are a crucial step within the framework of a direct recycling strategy for scrap Nd–Fe–B magnets.

Acknowledgements

This work was done as a part of the German joint project EnerGieeffziENtE Kreislaufwirtschaft kritischer Rohstoffe (GENESIS). Project partners included RWTH Aachen University for the crushing of scrap Nd–Fe–B, Ruhr-Universität Bochum for EDS processing of Nd–Fe–B scrap, Forschungszentrum Jülich for processing of Nd–Fe–B scrap via field-assisted sintering technology/spark plasma sintering (SPS) and flash SPS, and WILO SE for providing out-of-spec magnet material and conducting magnetic analysis. Furthermore, important input came from TU Darmstadt in the interpretation of the functional properties of recycled magnets. The GENESIS project was funded by German Federal Ministry for Economic Affairs and Climate Action (BMWK) according to a decision of the German Federal Parliament in the framework of the project “GENESIS—EnerGieeffziENtE Kreislaufwirtschaft kritischer Rohstoffe”, Förderkennzeichen 03EI5009D”. Funding is highly acknowledged. Experimental support and input of Ralf Steinert, Andrea Hilgers, Lukas Schäfer, and Dr. Stephan Küppers are highly acknowledged.

Open Access funding enabled and organized by Projekt DEAL.

Conflict of Interest

The authors declare no conflict of interest.

Data Availability Statement

The data that support the findings of this study are available from the corresponding author upon reasonable request.

Keywords

circular economy, field assisted sintering, functional materials, permanent magnets, rare earth elements, recycling

Received: August 31, 2023

Revised: October 13, 2023

Published online: October 26, 2023

-
- [1] O. Gutfleisch, M. A. Willard, E. Brück, C. H. Chen, S. G. Sankar, J. P. Liu, *Adv. Mater.* **2010**, *23*, 821.
- [2] Y. Matsuura, *J. Magn. Magn. Mater.* **2006**, *303*, 344.
- [3] S. Sugimoto, *J. Phys. D: Appl. Phys.* **2011**, *44*, 064001.
- [4] E. Alonso, A. M. Sherman, T. J. Wallington, M. P. Everson, F. R. Field, R. Roth, R. E. Kirchain, *Environ. Sci. Technol.* **2012**, *46*, 3406.
- [5] H. Kara, A. Chapman, T. Crichton, P. Willis, N. Morley, *Lanthanide Resources and Alternatives*, Oakdene Hollins Research and Consulting, Aylesbury, UK **2010**.
- [6] V. Balaram, *Geosci. Front.* **2019**, *10*, 1285.
- [7] Y. Bian, S. Guo, L. Jiang, J. Liu, K. Tang, W. Ding, *ACS Sustainable Chem. Eng.* **2016**, *4*, 810.
- [8] Z. Hua, J. Wang, L. Wang, Z. Zhao, X. Li, Y. Xiao, Y. Yang, *ACS Sustainable Chem. Eng.* **2014**, *2*, 2536.
- [9] J. A. Bogart, C. A. Lippincott, P. J. Carroll, E. J. Schelter, *Angew. Chem., Int. Ed.* **2015**, *54*, 8222.
- [10] I. Makarova, E. Soboleva, M. Osipenko, I. Kurilo, M. Laatikainen, E. Repo, *Hydrometallurgy* **2020**, *192*, 105264.
- [11] J. A. Bogart, B. E. Cole, M. A. Boreen, C. A. Lippincott, B. C. Manor, P. J. Carroll, E. J. Schelter, *Proc. Natl. Acad. Sci.* **2016**, *113*, 14887.
- [12] H. Fang, B. E. Cole, Y. Qiao, J. A. Bogart, T. Cheisson, B. C. Manor, P. J. Carroll, E. J. Schelter, *Angew. Chem.* **2017**, *129*, 13635.
- [13] M. Yue, X. Yin, W. Liu, Q. Lu, *Chin. Phys. B* **2019**, *28*, 077506.
- [14] R. K. Mishra, E. G. Brewer, R. W. Lee, *J. Appl. Phys.* **1988**, *63*, 3528.
- [15] J. J. Croat, *J. Common Met.* **1989**, *148*, 7.
- [16] X. J. Zhang, P. J. McGuinness, I. R. Harris, *J. Appl. Phys.* **1991**, *69*, 5838.
- [17] Y. Zhang, M. Liu, S. Sun, X. Yin, Y. Yin, J. Guo, W. Liu, D. Zhang, M. Yue, *J. Magn. Magn. Mater.* **2019**, *475*, 465.
- [18] M. A. Recai Önal, S. Dewilde, M. Degri, L. Pickering, B. Saje, S. Riaño, A. Walton, K. Binnemans, *Green Chem.* **2020**, *22*, 2821.
- [19] Y. Yang, A. Walton, R. Sheridan, K. Güth, R. Gauß, O. Gutfleisch, M. Buchert, B.-M. Steenari, T. Van Gerven, P. T. Jones, K. Binnemans, *J. Sustainable Metall.* **2017**, *3*, 122.
- [20] M. Schönfeldt, O. Diehl, E. Brouwer, K. Opelt, J. Gassmann, O. Gutfleisch, in *Conf. on Future Automotive Technology (CoFAT) 2018*, München, Germany, May **2018**.
- [21] M. Schönfeldt, U. Rohrmann, P. Schreyer, M. Hasan, K. Opelt, J. Gassmann, A. Weidenkaff, O. Gutfleisch, *J. Alloys Compd.* **2023**, *939*, 168709.
- [22] O. Diehl, M. Schönfeldt, E. Brouwer, A. Dirks, K. Rachut, J. Gassmann, K. Güth, A. Buckow, R. Gauß, R. Stauber, O. Gutfleisch, *J. Sustainable Metall.* **2018**, *4*, 163.
- [23] M. Zakotnik, I. R. Harris, A. J. Williams, *J. Alloys Compd.* **2009**, *469*, 314.
- [24] A. Habibzadeh, M. A. Kucuker, M. Göknelma, *ACS Omega* **2023**, *8*, 17431.
- [25] M. Zakotnik, E. Devlin, I. R. Harris, A. J. Williams, *J. Iron Steel Res. Int.* **2006**, *13*, 289.
- [26] R. S. Sheridan, I. R. Harris, A. Walton, *J. Magn. Magn. Mater.* **2016**, *401*, 455.
- [27] A. Lixandru, I. Poenaru, K. Güth, R. Gauß, O. Gutfleisch, *J. Alloys Compd.* **2017**, *724*, 51.
- [28] X. Li, M. Yue, M. Zakotnik, W. Liu, D. Zhang, T. Zuo, *J. Rare Earths* **2015**, *33*, 736.
- [29] O. Gutfleisch, K. Güth, T. G. Woodcock, L. Schultz, *Adv. Energy Mater.* **2013**, *3*, 151.
- [30] J. M. D. Coey, K. O'Donnell, *J. Appl. Phys.* **1997**, *81*, 4810.
- [31] R. Nakayama, T. Takeshita, M. Itakura, N. Kuwano, K. Oki, *J. Appl. Phys.* **1994**, *76*, 412.
- [32] O. Gutfleisch, *J. Phys. Appl. Phys.* **2000**, *33*, 157.
- [33] Y. Une, M. Sagawa, *J. Jpn. Inst. Met.* **2012**, *76*, 12.
- [34] K. Hioki, *Sci. Technol. Adv. Mater.* **2021**, *22*, 72.
- [35] R. K. Mishra, *J. Appl. Phys.* **1987**, *62*, 967.
- [36] L. Leich, A. Röttger, R. Kuchenbecker, W. Theisen, *J. Mater. Sci.: Mater. Electron.* **2020**, *31*, 20431.
- [37] T. Prasad Mishra, L. Leich, M. Krengel, S. Weber, A. Röttger, M. Bram, *Adv. Eng. Mater.* **2023**, *25*, 2201027.
- [38] E. Castle, R. Sheridan, W. Zhou, S. Grasso, A. Walton, M. J. Reece, *Sci. Rep.* **2017**, *7*, 11134.
- [39] F. Maccari, T. P. Mishra, M. Keszler, T. Braun, E. Adabifiroozjahi, I. Radulov, T. Jiang, E. Bruder, O. Guillon, L. Molina-Luna, M. Bram, O. Gutfleisch, *Adv. Eng. Mater.* **2023**, *25*, 2300252.
- [40] P. Nothnagel, K.-H. Müller, D. Eckert, A. Handstein, *J. Magn. Magn. Mater.* **1991**, *101*, 379.
- [41] B. E. Davies, R. S. Mottram, I. R. Harris, *Mater. Chem. Phys.* **2001**, *67*, 272.

- [42] L. Leich, A. Röttger, W. Theisen, M. Kregel, *J. Magn. Magn. Mater.* **2018**, 460, 454.
- [43] L. Leich, A. Röttger, M. Kregel, W. Theisen, *J. Sustainable Metall.* **2019**, 5, 107.
- [44] L. Zha, Z. Lin, F. Wang, Z. Liu, M. Xue, J. Yang, W. Yang, G. Tian, J. Han, C. Wang, H. Du, Y. Yang, J. Yang, *J. Magn. Magn. Mater.* **2020**, 514, 167128.
- [45] Arnold Magnetic Technologies, <https://www.arnoldmagnetics.com/wp-content/uploads/2019/06/Arnold-Neo-Catalog.pdf> (accessed: July 2023).
- [46] D. Brown, B.-M. Ma, Z. Chen, *J. Magn. Magn. Mater.* **2002**, 248, 432.
- [47] T. Sakagami, K. Ogura, *Trans. Jpn. Soc. Mech. Eng., Ser. A* **1992**, 58, 2224.
- [48] J. Orellana, I. Moreno-Villoslada, R. K. Bose, F. Picchioni, M. E. Flores, R. Araya-Hermosilla, *Polymers* **2021**, 13, 649.
- [49] T. J.-C. Liu, *Eng. Fract. Mech.* **2014**, 123, 2.
- [50] X. D. Xu, H. Sepehri-Amin, T. T. Sasaki, M. Soderžnik, X. Tang, T. Ohkubo, K. Hono, *Scr. Mater.* **2019**, 160, 9.
- [51] K. Niitsu, A. Sato, T. T. Sasaki, R. Sawada, Y. Cho, Y. Takada, T. Sato, Y. Kaneko, A. Kato, T. Ohkubo, D. Shindo, K. Hono, Y. Murakami, *J. Alloys Compd.* **2018**, 752, 220.
- [52] J. Liu, R. Xie, A. Aubert, L. Schäfer, H. Zhang, O. Gutfleisch, K. Skokov, *Appl. Phys. Lett.* **2023**, 122, 242402.
- [53] T. Zhang, W. Xing, F. Chen, L. Zhang, R. Yu, *Intermetallics* **2022**, 145, 107558.
- [54] R.-Q. Liu, W.-T. Guo, S. Zhang, G. Fu, Q. Huang, Y. Zheng, S. Chen, J.-M. Zhang, Z. Huang, *J. Magn. Magn. Mater.* **2023**, 587, 171242.
- [55] Magnequench, <https://mqitechnology.com/products/magnets/magnetic-properties> (accessed: July 2023).